1

2   Estimation of Liquid Water Path below the Melting Layer in Stratiform Precipitation Systems

3   using Radar Measurements during MC3E

4

5   Jingjing Tian[1], Xiquan Dong[1], Baike Xi[1], Christopher R. Williams[2], and Peng Wu[1]

6

7   [1]Department of Hydrology and Atmospheric Sciences, University of Arizona, Tucson, Arizona,

8   USA

9   [2] Department of Ann and H.J. Smead Aerospace Engineering Sciences, University of Colorado
10   Boulder
11

12

13   Manuscript Submitted to Atmospheric Measurement Techniques
14

15

16   Corresponding author address: Dr. Xiquan Dong, The Department of Hydrology and Atmospheric

17   Sciences, University of Arizona, 1133 E. James Rogers Way, Tucson, AZ 85721-0011.

18   Email: xdong@email.arizona.edu; Phone: 520-621-4652

19

20 **Abstract**

21 In this study, the liquid water path (LWP) below the melting layer in stratiform precipitation

22 systems is retrieved, which is a combination of rain liquid water path (RLWP) and cloud liquid

23 water path (CLWP). The retrieval algorithm uses measurements from the vertically pointing

24 radars (VPRs) at 35 GHz and 3 GHz operated by the U.S Department of Energy Atmospheric

25 Radiation Measurement (ARM) and National Oceanic and Atmospheric Administration (NOAA)

26 during the field campaign Midlatitude Continental Convective Clouds Experiment (MC3E). The

27 measured radar reflectivity and mean Doppler velocity from both VPRs and spectrum width from

28 the 35 GHz radar are utilized. With the aid of the cloud base detected by ceilometer, the LWP in

29 the liquid layer is retrieved under two different situations: (I) no cloud exists below the melting

30 base, and (II) cloud exists below the melting base. In (I), LWP is primarily contributed from

31 raindrops only, i.e., RLWP, which is estimated by analyzing the Doppler velocity differences

32 between two VPRs. In (II), cloud particles and raindrops coexist below the melting base. The

33 CLWP is estimated using a modified attenuation-based algorithm. Two stratiform precipitation

34 cases (20 May 2011 and 11 May 2011) during MC3E are illustrated for two situations, respectively.

35 With a total of 13 hours of samples during MC3E, statistical results show that the occurrence of

36 cloud particles below the melting base is low (9%), however, the mean CLWP value can be up to

37 0.56 kg m^{-2}, which is much larger than the RLWP (0.10 kg m^{-2}). When only raindrops exist below

38 the melting base, the averaged RLWP value is larger (0.32 kg m^{-2}) than the with cloud situation.

39 The overall mean LWP below the melting base is 0.34 kg m^{-2} for stratiform systems during MC3E.

40

41

1. Introduction

43   Clouds in stratiform precipitation systems are important to the Earth's radiation budget.

44 The vertical distributions of cloud microphysics, ice and liquid water content (IWC/LWC),

45 determine the surface and top-of-the-atmosphere radiation budget and redistribute energy in the

46 atmosphere (Feng et al., 2011; 2018). Also, stratiform precipitation systems are responsible for

47 most tropical and midlatitude precipitation during summer (Xu, 2013). However, the

48 representation of those systems in global climate and cloud-resolving models is still challenging

49 (Fan et al., 2015). One of the challenges is due to the lack of comprehensive observations and

50 retrievals of cloud microphysics (e.g. prognostic variables IWC and LWC) in stratiform

51 precipitation systems. Liquid water path (LWP), defined as an integral of LWC in the atmosphere.

52 It is a parameter used to provide the characterization of liquid hydrometeors in the vertical column

53 of atmosphere and study clouds and precipitation. The estimation of LWC/LWP is one of the

54 critical objectives of the US Department of Energy's (DOE) Atmospheric Radiation Measurement

55 (ARM) Program (Ackerman and Stokes, 2003).

56   LWP can be retrieved using the ground-based MicroWave Radiometer (MWR) sensed

57 downwelling radiant energy at 23.8 and 31.4 GHz (Liljegreen et al., 2001). In last two decades,

58 ARM has been operating a network of 2-channel (23.8- and 31.4-GHz) ground-based MWR to

59 provide a time series of LWP at the ARM Southern Great Plains (SGP) site (Cadeddu et al., 2013).

60 Absorption-based algorithms using multichannels of MWRs have been widely used to retrieve

61 cloud LWP (e.g., Liljegren et al. 2001; Turner, 2007), and they are known to be accurate methods

62 to estimate LWP of nonprecipitating clouds with mean LWP error of 15 g m^{-2} (Crewell and Löhnert,

63 2003). However, in precipitating conditions, LWP retrieved from conventional MWR are

64 generally not valid due to the violation of the Rayleigh assumption when large raindrops exist (e.g.,

65 Saavedra et al., 2012). In addition, large increase of brightness temperatures is measured as a

66 result of the deposition of raindrops on the MWR's radome. Unfortunately, it is very hard to model

67 and quantify this increase from rain layer on the radome (Cadeddu et al., 2017). This "wet-radome"

68 issue largely inhibits the retrieving of LWPs using ground-based MWR during precipitation. Due

69 to the limitations of retrieving LWP from MWR during precipitation, cloud and precipitation

70 radars were used to simultaneously retrieve LWP (Matrosov, 2010).

71   In the precipitating system, the liquid water cloud droplets and raindrops often coexist in

72 the same atmospheric layer (e.g., Dubrovina, 1982; Mazin, 1989; Matrosov, 2009, 2010),

73 indicating that the LWP consists of both cloud liquid water path (CLWP) and rain liquid water

74 path (RLWP). However, the discrimination between suspended small cloud liquid water droplets

75 and precipitating large raindrops is a very challenging remote sensing problem. Even though the

76 partitioning of LWP into CLWP and RLWP is important in cloud modeling (Wentz and Spencer,

77 1998; Hillburn and Wentz, 2008), there are few studies retrieved RLWP and CLWP

78 simultaneously and separately (Saavedra et al., 2012; Cadeddu et al., 2017). Battaglia et al. (2009)

79 developed an algorithm to retrieve RLWP and CLWP from the six Advanced Microwave

80 Radiometer for Rain Identification (ADMIRARI) observables under rainy conditions. Saavedra

81 et al (2012) developed an algorithm using both ADMIRARI and a micro rain radar to retrieve and

82 analyze the CLWP and RLWP for midlatitude precipitation during fall. In addition to these RLWP

83 and CLWP estimations mainly from passive microwave radiometers, there are several studies to

84 estimate the LWP using active radar measurements only. Ellis and Vivekanandan (2011)

85 developed an attenuation-based technique to estimate LWC, which is the sum of cloud water

86 contents (CLWC) and rain liquid water contents (RLWC), using simultaneous S- and Ka-band

87   scanning radars measurements. However, it is not always applicable of using these techniques to

88   retrieve LWC. If raindrop diameters are comparable to at least one of the radars' wavelength,

89   "Mie effect" will be included in the measured differential reflectivity, however this "Mie effect"

90   is not very distinguishable from differential attenuation effects (Tridon et al., 2013; Tridon and

91   Battaglia 2015).

92   Matrosov (2009) developed an algorithm to simultaneously retrieve CLWP and layer-mean

93   rain rate using the radar reflectivity measurements from three ground-based W-, Ka-, S- bands

94   radars. The CLWP were retrieved based on estimating the attenuation of cloud radar signals

95   compared to S-band radar measurements. Matrosov (2010) developed an algorithm to estimate

96   CLWP using a vertical pointing Ka-band radar and a nearby scanning C-band radar. The layer-

97   mean rain rate was first estimated with the aid of surface disdrometer, and then CLWP was

98   retrieved by subtracting the rain attenuation from total attenuation measured from two radars. For

99   the estimation of RLWP, Williams et al. (2016) developed a retrieval algorithm for rain drop size

100   distribution (DSD) using doppler spectrum moments observed from two collocated vertical

101   pointing radar (VPRs) at frequencies of 3 GHz and 35 GHz. The retrieved air motion and DSD

102   parameters were evaluated using the retrievals from a collocated 448-MHz VPR.

103   In this study, the CLWP retrieval algorithms in Matrosov (2009 and 2010) have been

104   modified given the available radar measurements, vertical pointing Ka- and S-band radars, during

105   the Midlatitude Continental Convective Clouds Experiment (MC3E) field campaign. For the

106   estimation of RLWP, we will basically follow the idea described in Williams et al. (2016) to

107   retrieve microphysical properties for raindrops. However instead of retrieving vertical air motion

108   and rain DSDs (Williams et al., 2016), this study aims at retrieving RLWCs, and then integrating

109   RLWCs over the liquid layer to estimate RLWP. Overall, in this study, algorithms from three

110   former publications are modified and combined to estimate the LWP in the stratiform precipitating

111   systems.

112   The goals of this study are to retrieve the LWP below the melting base, which includes

113   both RLWP and CLWP retrievals using radars measurements, and tentatively answer two

114   questions based on observations and retrievals in the stratiform precipitation systems during MC3E:

115   (1) what is the occurrence of cloud below the melting base in the stratiform precipitation systems;

116   (2) what are the values of simultaneous CLWP, RLWP and LWP, and how does CLWP or RLWP

117   contribute to the LWP.   Note that the CLWP and RLWP are constrained in a stratiform

118   precipitation layer below the melting base and above the surface. The LWP estimations in this

119   study are primarily aimed at stratiform precipitating events exhibiting melting-layer features from

120   radar measurements with lower-to-moderate rain rates (RR < 10 mm hr^{-1}). The instruments and

121   data used in this study are introduced in section 2. Section 3 describes the methods of retrieving

122   LWP (both RLWP and CLWP). Section 4 illustrates two examples and followed by statistical

123   results from more samples during MC3E. The last section gives the summary and conclusions.

124   Acronyms and abbreviations are listed in Table 1.

125

126   **2. Data**

127   The MC3E field campaign, co-sponsored by the NASA Global Precipitation Measurement

128   and the U.S. DOE ARM programs, was conducted at the ARM SGP (northern Oklahoma) during

129   April-June 2011 to study convective clouds and improve model parametrization (Jensen et al.,

130   2015). MC3E provided an opportunity to develop new retrieval methods to estimate cloud

131   microphysics and precipitation properties in precipitation systems (Giangrande et al., 2014;

132   Williams, 2016; Tian et al., 2016; Tian et al, 2018). Several stratiform rain cases were observed

133   by the VPRs during MC3E (as shown in Fig. 1). Distinct signatures of "bright band" are detected

134   from VPRs. To retrieve LWP associated with stratiform precipitation, this study mainly uses the

135   observations from two co-located VPRs operating at 3-GHz and 35-GHz at DOE ARM SGP

136   Climate Research Facility.

137   **2.1 Vertical Pointing Radars**

138   The 3-GHz (S-band) VPR was deployed by NOAA Earth System Research Laboratory for

139   the six-weeks during the MC3E. The NOAA 3-GHz VPR is a vertical pointing radar with 2.6°

140   beamwidth monitoring precipitation overhead. This 3-GHz profiler bridges the gap between cloud

141   radars, which are used to provide the structure of nonprecipitating clouds but are severely

142   attenuated by rainfall, and precipitation radars, which, although unattenuated by rainfall, generally

143   lack the sensitivity to detect more detailed cloud structure. The 3-GHz VPR observes the raindrops

144   within the Rayleigh scattering regime and its signal attenuation are negligible through the rain.

145   The temporal resolution of the profiles of Doppler velocity spectra is 7 seconds and the vertical

146   resolution is 60 meters. The 3-GHz VPR operated in two modes: a precipitation mode and a low-

147   sensitivity mode. The precipitation mode observations are used in this study.

148   The Ka-band ARM zenith radar (KAZR) is also a vertical pointing radar, operating at 35

149   GHz permanently deployed by DOE ARM at the SGP site. The KAZR measurements include

150   reflectivity, vertical velocity, and spectral width from near-ground to 20 km. The KAZR data used

151   in this study are the KAZR Active Remote Sensing of Clouds (ARSCL) product produced by the

152   ARM (www.arm.gov). The KAZR-ARSCL corrects for atmospheric gases attenuation and

153   velocity aliasing. By selecting the mode with the highest signal-to-noise ratio at a given point,

154   data from two simultaneous operating modes (general and cirrus mode) are combined for each

155   profile to provide the "best estimates" of radar moments in the time-height fields. The vertical and

156   temporal resolutions of KAZR-ARSCL product are 30 meters and 4 seconds, respectively. Since

157   the 3-GHz and 35-GHz VPRs are independent radars with different dwell time and sample

158   volumes (Williams et al., 2016), the radar observations are processed to 1-min temporal and 60-m

159   vertical resolutions in this study.

160   **2.2 Disdrometers**

161   DOE ARM program maintains a suite of surface precipitation disdrometers.

162   Measurements and estimations from the Distromet model RD-80 disdrometer and NASA two-

163   dimensional video disdrometers (2DVD) deployed at the ARM SGP site are used in this study.

164   The RD-80 disdrometer provides the most continuous raindrop size distribution (DSD)

165   measurements at high spectral (20 size bins from 0.3 to 5.4 mm) and temporal resolutions (1

166   minute), and its minimal detectable precipitation amount is 0.006 mm hr^{-1}. From 2DVD, the rain

167   DSDs are observed from 41 bins (0.1 - 10 mm), and its minimal detectable precipitation amount

168   is 0.01 mm hr^{-1}. In addition to rain rate, the mean mass-weighted raindrop diameter (D_m) is also

169   provided from 2DVD, which is used for evaluating retrieved D_m from radar measurements.

170   **2.3 Ceilometer**

171   A Vaisala laser ceilometer (CEIL) operates at the SGP Central Facility, sensing cloud

172   presence up to a height of 7700m with 10-m vertical resolution. The laser ceilometer transmits

173   near-infrared pulses of light, and the receiver detects the light scattered back by clouds and

174   precipitation. It is designed to measure cloud-base height.

175

176   **3. The Methodology of Liquid Water Path Estimation**

177   As mentioned earlier, both RLWP and CLWP contribute to the LWP. With the aid of the

178   cloud base height detected by ceilometer, LWP is retrieved under two different situations: (I) the

179   cloud base is higher than the melting base and (II) the cloud base is lower than the melting base.

180   For situation (I), there are almost no cloud droplets below melting base (CLWP = 0), and thus the

181   LWP below the melting base is solely from raindrops. The LWP is calculated by integrating

182   RLWCs over this layer. The RLWCs could be retrieved by analyzing the measured Doppler

183   Velocity Differences ("*DVD Algorithm*") from two collocated VPRs. In situation (II), the small

184   cloud droplets and large raindrops coexist below the melting base. Both raindrops and cloud

185   particles contribute to LWP. RLWP will be still estimated using "*DVD Algorithm*". CLWP will

186   be retrieved using an attenuation-based algorithm named as "*Attenuation Algorithm*". The

187   algorithms for LWP estimation are summarized in a flowchart (Fig. 2).

188   **3.1 Situation I (no cloud droplets exist below the melting base)**

189   The algorithm from Williams et al. (2016) was developed based on an assumption that the

190   3-GHz VPR operates within the Rayleigh scattering regime for all raindrops, while the 35-GHz

191   VPR operates within the Rayleigh scattering regime for small raindrops (diameters < ~1.3 mm)

192   and non-Rayleigh scattering regime for larger raindrops (diameters ≥ ~1.3 mm). The different

193   scattering regimes for the two operating frequencies result in different estimated radar moments.

194   These estimated radar moments are in functions of rain microphysics. Thus, the rain microphysics

195   could be retrieved with given measured radar moments.   The details of this "*DVD Algorithm*"

196   and uncertainty estimation are introduced in Appendix A.

197   **3.2 Situation II (cloud particles and rain droplets coexist below the melting base)**

198   In situation (II), substantial cloud particles exist below melting base, and both RLWP and

199   CLWP retrievals are needed to estimate the LWP. The total two-way attenuation of 35-GHz VPR

200   signals, A (in decibels, dB), in a layer between the melting base and the cloud base, mainly consists

201   of rain attenuation, liquid clouds attenuation, and gaseous attenuation. The total attenuation (A)

202   are expressed as:

$$A = 2\ C\ R_m\ \Delta H + 2\ B\ CLWP + G. \tag{1}$$

204   R_m is layer-mean rain rate, and ΔH (km) is the thickness of the layer (Matrosov, 2009).   G is the

205   two-way attenuation/absorption from atmospheric gases, which is relatively small, and the

206   absorption by gases has been already corrected in the KAZR ARSCL dataset and is assumed to be

207   zero in our retrieval.

208   C and B are the coefficients for rainfall and cloud liquid water attenuation.

$$B = 0.0026\pi\lambda^{-1} Im[-(m^2-1)(m^2+2)^{-1}], \tag{2}$$

210   where λ is the wavelength of Ka-band radar, and m is the complex refractive index of water. The

211   unit of B is dB/g m^{-2}.

$$C = 0.27\ b, \tag{3}$$

213   where b is the correction factor considering raindrop fall velocities with changing air density.

$$b = (\rho_{am}/\rho_{a0})^{0.45}, \tag{4}$$

215   where ρ_{am} and ρ_{a0} are the mean air density in the rain layer and the density at normal atmospheric

216   conditions.

217   Based on (1), CLWP can be written as:

$$CLWP = \frac{A - 2\ C\ R_m\ \Delta H - G}{2\ B} \tag{5}$$

219   The attenuation (A) is estimated by comparing the drop in Ka-band reflectivity with the

220   un-attenuated S-band reflectivity through the cloud. Assuming the changes in reflectivity with

221   altitude due to changes in raindrop size distributions with altitude are similar for Ka- and S-band

222   reflectivities, then the difference in reflectivities through the cloud is a proxy for attenuation. This

223   can be expressed using

224 $$A \cong [Z_{Ka}(cloud\ base) - Z_{Ka}(melting\ base)] - [Z_S(cloud\ base) - Z_S(melting\ base)] \quad (6)$$

225 Notice that the absolute calibration of the radar was not important to the retrieval results since the

226 retrieval of CLWP used S-Ka differential attenuation. This avoids the radar calibration (Tridon et

227 al., 2015 and 2017), which is a serious issue limiting the accuracy of radar retrievals.

228   The R_m is estimated as:

229 $$R_m = \frac{\sum_{h0}^{MB} RR(h) \times \Delta h}{\Delta H}, \quad (7)$$

230 where Δh equals 60 meters and MB is the melting base and h_0 is the height of the lowest unsaturated

231 KAZR rang gate (Matrosov, 2010). RRs in the layer between the melting base and the cloud base

232 are calculated from the "*DVD algorithm*".

233   The uncertainties of retrieved CLWP are mainly due to the uncertainties of estimated R_m

234 and observed total attenuation from VPRs. The value of B is on the order of 1 dB/kg m^{-2}. The

235 uncertainty of retrieved CLWP would be ~ 0.25 kg m^{-2} with 0.5 dB uncertainty from measured

236 radar reflectivity difference or ~ 0.5 kg m^{-2} for 1.0 mm hr^{-1} uncertainty from estimated layer-mean

237 rain rate. Compared to the typical mean rain rate observed in the stratiform system (~ 2 - 4 mm

238 hr^{-1}), 1.0 mm hr^{-1} represents a ~ 30% uncertainty. The uncertainty for CLWP retrievals is roughly

239 estimated as ~ 0.56 kg m^{-2} (sqrt ($0.25^2 + 0.5^2$)) in this study. For reference, the expected uncertainty

240 is reported as ~ 0.25 kg m^{-2} for typical rainfall rates (~ 3 - 4 mm hr^{-1}) in Matrosov (2009) retrieval

241 method. More details of the estimation of CLWP uncertainties are in Appendix B.

242 **4. Retrieval Results and Discussions**

243 **4.1 Case Studies**

244   Even though situation (I) is dominated (Fig. 1), especially in Case A, the ceilometer cloud

245 base estimates can be lower than the melting base (Cases B to D). Two case studies (20 May 2011

246 and 11 May 2011) are given as examples to demonstrate the estimation of LWP in stratiform

247 precipitation system for two different situations.

248 **4.1.1 Case A**

249   On 20 May 2011, an upper level low-pressure system at central Great Basin moved into

250 the central and northern Plains, while a surface low pressure at southeastern Colorado brought the

251 warm and moist air from the southern Plains to a warm front over Kansas. and a dry line extended

252 southward from the Texas-Oklahoma. With those favorable conditions, a strong north-south

253 oriented squall line developed over Great Plains and propagated eastward. The convection along

254 the leading edge of this intense squall line exited the ARM SGP network around 11 UTC 20 May

255 leaving behind a large area of stratiform rain (Case A in Fig. 1). This stratiform system passed

256 over the ARM SGP site and observed by two VPRs, and disdrometers as shown in Figures 1a-1c.

257 It clearly shows the 3-GHz radar echo tops are much lower than those from the 35 GHz VPR.

258 Even though there is attenuation at 35-GHz by the raindrops and melting hydrometeors, the 35-

259 GHz radar can still detect more small ice particles at near the cloud top. The "bright band", which

260 occurs in a uniform stratiform rain region, is clearly seen from the 3-GHz VPR (a sudden increase

261 and then decrease in radar reflectivity) but is not obvious from the 35-GHz VPR due to the non-

262 Rayleigh scattering effects at 35 GHz (Sassen et al., 2005; Matrosov, 2008).

263   Figures 1a-1b clearly show that the ceilometer detected cloud base is in the middle of the

264 melting layer, indicating almost no cloud particles below the melting layer and the LWP in the

265 liquid layer equals to RLWP. The RLWP is retrieved using the "*DVD Algorithm*" introduced in

266 section 3.1 and Appendix A. Figure 3 shows an example of the DVD retrieval algorithm at 13:40

267 UTC on May 20, 2011. Radar reflectivity from 3 GHz, Doppler velocities from 3 GHz and 35

268 GHz, and spectrum variance from 35 GHz are the inputs of DVD algorithm. The Doppler velocity

269   differences (3 GHz – 35 GHz) from the surface to 4 km are also plotted in Fig. 3d. The melting

270   base is defined as the height of maximum curvature in the radar reflectivity profile at 3 GHz (Fabry

271   and Zawadzki, 1995), which is clearly seen at 2.5 km in Fig. 3. Below 2.5 km, the Doppler velocity

272   differences between the two VPRs become relatively uniform, indicating that the process of

273   melting snow/ice particles into raindrops is completed. Retrieved profiles of rain microphysical

274   properties and their corresponding uncertainties (horizontal bars at different levels) in the rain layer

275   (0 – 2.5 km) are shown in Figs 3f-3h. In general, the retrieved D_m values from the surface to 2.5

276   km are nearly a constant of ~2 mm (Fig. 3f), while the retrieved RLWC and rain rate values slightly

277   decrease from 2.5 km to the surface. One of the highlights of this study is, in addition to the surface

278   rain rate, which can usually be observed using surface disdrometers, the vertical profiles of rain

279   microphysical properties are retrieved. These retrieved rain microphysical properties will shed

280   light on the understanding of liquid cloud and rain microphysical processes (like condensation,

281   evaporation, autoconversion and accretion etc.) in the models.

282   To evaluate the rain property retrievals, we compare the retrieved rain microphysical

283   properties, the D_m, and rain rate at the surface, with the surface disdrometers measurements (Fig.

284   4). The D_m values range from 1.0 to 2.5 mm during a 3.5-hr period with nearly identical mean

285   values of 1.79 mm and 1.81 mm from both retrievals and 2DVD measurements. There are large

286   variations for rain rates, ranging from 0 to 8 mm hr^{-1}, with means of 3.19, 3.17 and 2.88 mm hr^{-1},

287   respectively, from 2DVD, RD-80 and radar retrieval. The mean rain rates from 2DVD and RD-

288   80 measurements are almost the same although there are relatively large differences during certain

289   time periods, while the retrievals from this study, on average, underestimate the rain rate by ~10%

290   compared to the disdrometer measurements. More statistics (mean differences, their 95%

291   confidence intervals of mean differences and root mean square errors) can be found in Table 2.

292 Overall, the mean differences are within the retrieval uncertainties. The variation of RLWP (Fig.

293 4c) mimics the variation of retrieved rain rate in Fig. 4d. The mean value of RLWP is 0.55 kg m^{-2}

294 ^{2} for this case, which is also the LWP below the melting base.

295 **4.1.2 Case B**

296 On 11 May 2011, a surface cold front moved across the Oklahoma-Texas area and then

297 convections were initiated. At 1600 UTC, a mesoscale convective system organized with a parallel

298 stratiform precipitation region. Two-three hours later (~1830 UTC), the mesoscale convective

299 system was transitioned to a trailing stratiform mode passed over the ARM SGP site.   The large

300 stratiform regions are observed by two VPRs and disdrometers as shown in Figs 1d-1f. Figures

301 1d-1f clearly show that the ceilometer detected cloud bases are lower than the melting bases

302 occasionally. Under this situation, both RLWP and CLWP could contribute to the LWP below the

303 melting base.

304 Firstly, the surface rain microphysics (D_m, RLWC, rain rate and RLWP) are retrieved using

305 "*DVD Algorithm*". These rain property retrievals are compared with the surface disdrometers

306 measurements (Fig. 5). The D_m values at the surface range from 0.90 to 2.30 mm during a 4.5-hr

307 period with the mean values of 1.41 mm and 1.52 mm, respectively, from both retrievals and

308 2DVD measurements. The difference between the retrieval and 2DVD measurement may be due

309 to different sampling volumes between radar and the surface disdrometer, as well as wind shear.

310 The rain rates, in this case, vary quite large, ranging from 0.02 to 4.78 mm hr^{-1} with means of 1.36,

311 1.26 and 1.66 mm hr^{-1}, respectively from single 2DVD, RD-80, and our retrieval. It is found that,

312 from both Case A and Case B, the mean value from RD-80 is smaller than that from 2DVD. This

313 may be due to the different ranges of measurable drop sizes from two types of disdrometers (0.3 -

314   5.4 mm for RD 80, while 0.1 to 10 mm for 2DVD). More statistics can be also found in Table 2.

315   Overall, the mean differences are still within the retrieval uncertainties for this case.

316   Secondly, the CLWP is retrieved using "Attenuation Algorithm" introduced in section 3.2.

317   Figure 5c shows the time series of RLWP, CLWP and LWP retrievals. It is found that the CLWP

318   values (when they exist) are usually larger than RLWP values in the same vertical column. When

319   cloud droplets and raindrops coexist below the melting base, the mean values are 0.11 kg m^{-2} and

320   1.64 kg m^{-2} for RLWP and CLWP, and the corresponding LWP below the melting layer is 0.76 kg

321   m^{-2}. While when only raindrops exist below the melting base, there is no CLWP (CLWP =0), and

322   the RLWP and LWP are the same (with average of 0.34 kg m^{-2}). It is noticed that even though the

323   occurrence of CLWP is low (11%) in this case, the value of CLWP can be very large when it exists,

324   and it is about two times larger than the mean RLWP. The mean value of LWP is 0.37 kg m^{-2} for

325   all the samples in Fig. 5c. The blue uncertainty bars in Figure 5c show the retrieved CLWP

326   uncertainty with assuming both of the uncertainties of attenuation and total rain rate are 30%. Due

327   to the variations of the attenuation and total rain rate with time, the estimated uncertainties of

328   CLWP varies point to point. More details about the estimation of CLWP are in Appendix B.

329

330   **4.2 Statistical Results**

331   Box and whisker plots of retrieved RLWP, CLWP and LWP for situations (I), (II) and all

332   samples during MC3E are shown in Fig. 6. The horizontal orange and red dashed lines indicate

333   the median and mean, boundaries of the box represent the first and third quartiles, and the whiskers

334   are the 10th- and 90th -percentiles. During MC3E, a total of 13 hours of stratiform rain were

335   observed by VPRs at the ARM SGP Climate Research Facility, in which 91% and 9% the samples

336   are categorized into the situations (I) and (II), respectively. The mean RLWPs are 0.32 kg m^{-2} and

337   0.10 kg m^{-2} for the situations (I) and (II). There are a substantial amount of small cloud droplets

338   sustaining in the rain layer and having not yet converted to larger raindrops, which may partially

339   explain smaller RLWP in the situation (II). The mean value of surface rain rate is 2.06 mm hr^{-1}

340   when cloud droplets exist, which is also smaller than the mean value (2.38 mm hr^{-1}) in the rain-

341   only situation. The mean CLWP in the situation (II) is as large as ~0.56 kg m^{-2} even though their

342   occurrence is very low (9%), which is much larger than mean RLWP in the liquid layer.   The

343   LWP from the situation (II) (0.66 kg m^{-2}) is much larger than the mean LWP from the situation (I)

344   (0.32 kg m^{-2}), which is primarily contributed by cloud droplets. The overall mean LWP for

345   stratiform rain during MC3E is 0.34 kg m^{-2}.

346   We also processed the ARM MWR retrieved LWPs during MC3E and compared them with

347   our retrievals as illustrated in Fig. 7a. The corresponding LWP uncertainties are also provided as

348   the grey error bar for each retrieval with rain rate indicated by colors. It is noticed that the MWR

349   has no LWP estimation when the rain rate is large. The MWR-retrieved LWPs increase with

350   increased rain rate, and the retrievals from MWR are much larger than the new LWP retrievals at

351   high rate rates. The newly retrieved LWPs weakly correlate with rain rates, and most values are

352   less than 1.0 kg m^{-2}, especially at high rain rates. The MWR retrieved LWPs increase with rain

353   rate generally. The increase of retrieved LWP with rain rate from MWR is possibly due to the

354   "wet radome" effect (Cadeddu et al., 2017). In addition to the issue from standing water on the

355   radome, the extinctions due to raindrops also affect MWR retrievals. The extinction for rain is

356   much larger than that for cloud (Sheppard, 1996), and thus, the small amount of rain water could

357   enhance the measured brightness temperature significantly. More details of extinctions and

358   brightness temperature calculations are shown in Appendix B. Statistical results of the retrieved

359   LWPs from this study and MWR are averaged for each measured rain rate bins (bin size = 0.25

360   mm hr⁻¹). The differences of LWPs from MWR and this study are shown in Fig. 7b. The LWP

361   differences increase with increased rain rate. The LWP differences between MWR retrieval and

362   this study could be caused by the following reasons. 1) MWR-retrieved LWP represents the entire

363   vertical column (RWLP and CLWP below melting layer, large water coated ice particles in the

364   melting layer and supercooled LWCs above the melting layer), while our retrieval only represents

365   the LWP below the melting base. As Battaglia et al (2003) pointed out the brightness temperature

366   generally increases if mixed-phase precipitation is included. 2) The MWR radome was wet during

367   the raining periods and the deposition of raindrops on the radome can cause a large increase in the

368   measured brightness temperatures (Cadeddu et al., 2017). 3) Large extinctions due to rain drops

369   would affect MWR retrievals.   4) Uncertainties exist in the retrieved LWP from this study.

370

371   **5. Summary and Conclusions**

372   LWP is a critical parameter for studying clouds, precipitation, and their life cycles. LWP

373   can be retrieved from microwave radiometer measured brightness temperatures during cloudy and

374   light precipitation conditions. However, MWR-retrieved LWPs are questionable under moderate

375   and heavy precipitation conditions due to the "wet radome" and the large extinction in the unit

376   volume caused by large raindrops. LWPs below the melting base in stratiform precipitation

377   systems are estimated, which include both RLWP and CLWP. The measurements used in this

378   study are mainly from two VPRs, 35-GHz from ARM and 3-GHz from NOAA during the MC3E

379   field campaign.

380   In this study, the microphysical properties of raindrops, such as D_m, RLWC (and RLWP),

381   and RR, are estimated following the method described in Williams et al. (2016) using

382   measurements from co-located Ka- and S-band radars VPRs. The retrieved rain microphysical

383   properties are validated by the surface disdrometer measurements. Instead of retrieving vertical

384   air motion and rain DSDs (Williams et al., 2016), this study aims at retrieving RLWCs and then

385   integrating RLWCs over the liquid layer to estimate RLWP. The CLWP is retrieved based on the

386   modifications of the methods in Matrosov (2009 and 2010) with available radar measurements,

387   vertical pointing Ka- and S-band VPRs, during the MC3E field campaign.

388   The applicability of retrieval methods is illustrated for two stratiform precipitation cases

389   (20 May 2011 and 11 May 2011) observed during MC3E. Statistical results from a total of 13

390   hours samples during MC3E show that the occurrence of cloud droplets below the melting base is

391   low (9%), while the CLWP value can be up to 0.56 kg m^{-2}, which is much larger than the RLWP

392   (0.10 kg m^{-2}). When only raindrops exist below the melting base, the averaged RLWP value is

393   0.32 kg m^{-2}, which is much larger than the mean RLWP in the cloud droplets and raindrops

394   coexisted situation. Our retrievals are also compared with ARM MWR retrieved LWPs. It is

395   noticed that the MWR has no LWP estimation when the rain rate is large. The MWR-retrieved

396   LWPs increase with increased rain rate, and the retrievals from MWR are much larger than our

397   LWP retrievals at high rate rates. The LWP differences are fully discussed.

398   Reliable retrievals of RLWC and RLWP are critical for model evaluation and improvement,

399   as RLWC (rain mixing ratio) is an important prognostic variable in weather and climate models.

400   Furthermore, the retrievals in the whole rain layer would be useful to understand the microphysical

401   processes (i.e., condensation, evaporation, autoconversion, and accretion etc.) and have great

402   potential to improve model parametrizations in the future. Overall, the LWP (CLWP and RLWP)

403   retrievals derived in this study can be used to evaluate the models that separately predict cloud and

404   precipitation and contribute comprehensive information to study cloud-to-precipitation transitions.

405   Note that the attenuation by liquid is more profound at 94 GHz and the ratio of attenuations by

406   liquid clouds and by rain is larger at 94 GHz compared to 35 GHz (Matrosov, 2009). Thus, using

407   94 GHz (W-band) radar measurements to develop a retrieval algorithm may be promising if the

408   W-band radar signals are not fully attenuated. In addition, analyzing collocated multiple-

409   frequency VPRs would also better define the uncertainties of retrievals made with collocated radar

410   operating at different frequency pairs.

411

412

413   **Appendix A: Doppler Velocity Differences Algorithm ("*DVD Algorithm*")**

414   Retrieving RLWC and other rain microphysical properties (i.e., drop size and rain rate) is

415   based on the mathematics of DSD radar reflectivity-weighted velocity spectral density S_{DSD}^{λ}

416   [(mm^6 m^{-3}) (m s^{-1})$^{-1}$], which is a product of radar raindrop backscattering cross section $\sigma_b^{\lambda}(D)$ (mm^2)

417   and DSD number concentration $N_{DSD}(D)$ (mm^{-1} m^{-3}):

$$S_{DSD}^{\lambda}(v_z) = [\frac{\lambda^4}{\pi^5 |K_w|^2} \sigma_b^{\lambda}] N_{DSD}(D) \frac{dD}{dv_z} . \tag{A1}$$

419   The $\frac{dD}{dv_z}$ [mm (m s^{-1})$^{-1}$] is used as a coordinate transformation from diameter to velocity, where

420   v_z (m s^{-1}) is the raindrop terminal velocity of diameter D (mm) at altitude z. λ is the wavelength

421   of radar. $|K_w|^2$ equals 0.93 and it is the dielectric factor.

422   The $N_{DSD}(D)$ can be expressed as a normalized gamma shape distribution with three parameters

423   (Leinonen et al., 2012):

$$N_{DSD}(D; N_w, D_m, \mu) = N_w f(D; D_m, \mu), \tag{A2}$$

425   where

$$f(D; D_m, \mu) = \frac{6}{4^4} \frac{(\mu+4)^{(\mu+4)}}{\Gamma(\mu+4)} (\frac{D}{D_m})^{\mu} \exp\left[-(\mu + 4)\frac{D}{D_m}\right]. \tag{A3}$$

427   N_w is the scaling parameter, μ is a shape parameter, $\Gamma(x)$ is the Euler gamma function, and D_m is

428   a mean mass-weighted raindrop diameter estimated from the ratio of the fourth to third DSD

429   moments:

430
$$D_m = \frac{M_4}{M_3} = \frac{\int_{D_{min}}^{D_{max}} N_{DSD}(D) D^4 dD}{\int_{D_{min}}^{D_{max}} N_{DSD}(D) D^3 dD} \; . \tag{A4}$$

431   where D_{min} and D_{max} represent the minimum and maximum diameters in the distribution,

432   respectively.

433   The intrinsic (non-attenuation) reflectivity factor and the mean velocity and the spectrum

434   variance are the zeroth, first, and second reflectivity-weighted velocity spectrum moments:

435
$$Z_{DSD}^{\lambda} = \sum_{v_{min}}^{v_{max}} S_{DSD}^{\lambda}(v_i) \Delta v \tag{A5}$$

436
$$v_{DSD}^{\lambda} = \frac{\sum_{v_{min}}^{v_{max}} S_{DSD}^{\lambda}(v_i) \, v_i \, \Delta v}{Z_{DSD}^{\lambda}} \tag{A6}$$

437
$$SV_{DSD}^{\lambda} = \frac{\sum_{v_{min}}^{v_{max}} (v_i - v_{DSD}^{\lambda})^2 S_{DSD}^{\lambda}(v_i) \, \Delta v}{Z_{DSD}^{\lambda}} . \tag{A7}$$

438   where v_i is the discrete velocities and Δv is velocity resolution in the integration.

439   The Doppler Velocity Difference (DVD) is defined as

440
$$DVD = v_{DSD}^{3\,GHz} - v_{DSD}^{35\,GHz} . \tag{A8}$$

441   Note that both DVD and SV are dependent on DSD parameters (D_m and μ) only.

442   The RLWC and rain rate (RR) can also be described using the DSD:

443
$$RLWC(g\,m^{-3}) = \frac{\pi}{6} 10^{-3} \sum_{D_{min}}^{D_{max}} N_{DSD}(D, N_w, D_m, \mu) D_i^3 \Delta D \tag{A9}$$

444
$$RR(mm\,hr^{-1}) = \frac{6\pi}{10^4} \sum_{D_{min}}^{D_{max}} N_{DSD}(D, N_w, D_m, \mu) D_i^3 v_z(D_i) \Delta D . \tag{A10}$$

445   In addition, there are two newly defined radar-related parameters (α and β), which are also

446   dependent on D_m and μ only:

447
$$\alpha = 10 \, \log_{10}(Z_{DSD}^{3GHz}/RLWC) \tag{A11}$$

448
$$\beta = 10 \log_{10}(Z_{DSD}^{3GHz}/RR) \tag{A12}$$

449   In this study, four variables, DVD, SV at 35 GHz (SV_{35GHz}), α and β, are pre-calculated

450   using different groups of D_m and μ values, and then these values are stored in look-up tables

451   (LUTs). Raindrop backscattering cross sections are calculated using the T-matrix with different

452   temperatures and oblate raindrop axis ratios (Leinonen, 2014). LUT examples are illustrated in

453   Fig. A as functions of DVD and SV_{35GHz}. If we assume that the observed radar Doppler velocity

454   difference and spectrum variance from the 35-GHz radar is equal to the DSD velocity difference

455   and variance (DVD and SV_{35GHz}), the measured Doppler velocity difference and spectrum variance

456   at 35-GHz can determine a solution for D_m from the LUT (Fig. A(a)). Similarly, a value of

457   Z_{3GHZ}LWC (or Z_{3GHZ}RR) can be found with measured DVD and SV_{35GHz} using the LUT in Fig. A(b)

458   (or Fig. A(c)). Then RLWC (or RR) can be estimated using (A11) (or (A12)) with measured

459   reflectivity at 3-GHz (Z_{3GHZ}).

460   The observed radar Doppler velocity difference can be assumed to be equal to the DSD

461   velocity difference for two reasons: (1) even though the radar observed Doppler velocity spectrum

462   can be broaden by the air motion, this spectrum broadening variance is small (within 2%) relative

463   to the DSD velocity spectrum because of the narrow beamwidth (0.2°) of KAZR and (2) spectrum

464   broadening is symmetric, which does not affect the first spectrum moment and the DSD mean

465   Doppler velocity only shifts due to the air motion. Therefore, the measured differences of Doppler

466   velocity between the 3-GHz and 35- GHz radars vertical pointing observations are independent of

467   air motion and can be assumed to be the same as DVD from (A8). The validity of such an

468   assumption is fully discussed in Williams et al. (2016).

469   The variabilities of 3-GHz and 35-GHz VPR observations within each 1-minute/60-meter

470   bin are regarded as the measurement uncertainties and will be propagated through the retrieval to

471   produce retrieval uncertainties. The retrieval uncertainties are estimated follow two steps: (1)

472   construct a distribution of input radar measurements. For example, the temporal resolution for 3-

473   GHz VPR is seven seconds, thus there are about nine radar reflectivities observed for one minute.

474   A normal distribution is generated first using the mean and standard deviations of these nine

475   observed radar reflectivities for this 1-min/60-m resolution/bin. (2) repeat the DVD retrievals

476   using samplings from distributions of all input measurements. We randomly select 100 groups of

477   members from those (DVD, SV_{35GHz}, Z_{3GHz}) normal distributions to form 100 realizations, and then

478   produce 100 separate output estimates. The mean and standard deviation of the 100 solutions are

479   regarded as the final retrieval and the retrieval uncertainty.

480   The uncertainties of RLWP are estimated based on the uncertainties of RLWC. More

481   specifically, we first estimated the RLWC uncertainties at each height level, and then we calculated

482   the ratios of RLWC uncertainties to the mean retrieved RLWCs at each height level, which

483   represent percentage values of retrieval uncertainties. Finally, we calculated the mean ratio of the

484   uncertainties in the whole liquid layer below melting base and regarded this mean ratio as the

485   uncertainty of RLWP.

486   It is noted that the uncertainty here only considers estimates of instrument noise, not the

487   uncertainties associated with assumptions used in the retrieval. For example, the gamma size

488   distribution used in (A2) is an approximation which may introduce error into the retrieval.

489   However, it is very difficult to quantify this type of retrieval uncertainty. In this study, we further

490   compared our retrievals with independent surface disdrometers measurements to estimate the

491   uncertainties of retrievals. Also, when both radars are observing at Rayleigh scattering for small

492   raindrops, the reflectivity-weighted radial velocities for these particles should be the same. In

493   order to have a difference in radial velocity during the retrieval, large droplets must exist. The

494 maximum diameters in drop size distribution measured from disdrometer for all the stratiform

495 cases during MC3E are investigated. It is found that the occurrence of small-droplets-only

496 (maximum diameter <1.3 mm) is very low (less than 3%). Thus, it will not have a significant

497 impact on the retrieval results. Notice that this algorithm is not suitable for strong convective rain

498 due to the wind shear and strong turbulence as well as severe attenuation and extinction of the Ka-

499 band radar signal.

500

501 **Appendix B: CLWP Uncertainty**

502   CLWP can be simplified and estimated as following equation:

503
$$\text{CLWP} = \frac{A - 2\,C\,R_{total}}{2\,B}. \tag{B1}$$

504 The attenuation (A) is estimated by comparing the drop in Ka-band reflectivity with the un-

505 attenuated S-band reflectivity. The rain attenuation is estimated by the rain attenuation coefficient

506 (C) multiplied by the total rain rate (R_{total}). C and B are the coefficients of rain and cloud water

507 attenuation with values of $\sim$ 0.26 dB /km /mm hr^{-1} and $\sim$ 0.87 dB / kg m^{-2}, respectively. The

508 influence of temperature uncertainty in B on the retrieval error is minor compared to the

509 uncertainties of the total attenuation (A) and total rain rate (R_{total}) (Matrosov 2010). The

510 uncertainty of CLWP is calculated as

511
$$\Delta CLWP = \sqrt{\left(\frac{\partial CLWP}{\partial A} \times \Delta A\right)^2 + \left(\frac{\partial CLWP}{\partial R_{total}} \times \Delta R_{total}\right)^2} \tag{B2}$$

512
$$\Delta CLWP = \sqrt{\left(\frac{1}{2B} \times A \times \Delta a\right)^2 + \left(-\frac{C}{B} \times R_{total} \times \Delta r\right)^2} \tag{B3}$$

513 For given uncertainties of attenuation (Δa) and total rain rate (Δr), the uncertainty of CLWP can

514 be calculated based on equation (B3).

515

516

517

518 **Appendix C: Calculations of Extinction and Brightness Temperature at Microwave**

519 **Radiometer Channels**

520   To better explain the "overestimation" issue of retrieved LWP from microwave radiometer,

521 several examples are given in this appendix. Firstly, we calculated the extinction cross section per

522 volume as a function of the drop equivolume diameter for the two frequencies in MWR (23.8 GHz

523 and 31.4 GHZ) with a T-matrix method (Figure B). It is clearly shown that the extinction cross

524 section is increasing with the diameter when the diameter is smaller than 3 mm. This indicates the

525 extinction (cross section) for rain drops (diameter $> \sim$ 50 um) is much larger than that for cloud

526 droplets (diameter $< \sim$50 um). Secondly, we calculated the extinction coefficient as a function of

527 RLWC for populations with three different drop size distributions (DSDs). The DSDs are modeled

528 according to the exponential Marshall and Palmer (MP) distribution $N(D) = N_0 \, e^{-\Lambda D}$, where

529 $N_0=8000$ m^{-3} mm^{-1}. N_0 is changed to 4000 and 32000 m^{-3} mm^{-1} to represent thunderstorm and

530 drizzle DSDs. More details of the DSDs please see Battaglia et al. (2009). Figure C clearly shows

531 the extinctions of cloud and rain also is DSD-dependent. For example, at 31.4 GHz, even though

532 the RLWC is the same, the extinctions are much larger from the precipitation with the

533 thunderstorms and MP DSDs than the extinctions from light precipitation with the drizzle DSD.

534   In addition, the brightness temperatures at 23.8 and 31.4 GHz channels are calculated using

535 the MicroWave Radiative Transfer (MWRT) model. Five different sensitivity tests are generated

536 with five combinations of CLWP and RLWP values (Table A). Table A lists the results and clearly

537 demonstrates that the brightness temperatures in channels increase with increased cloud water

538 amount (larger CLWP) and the rain water amount (larger RLWP). Comparing the results from

539   test #2 and #3, it is clearly seen that the brightness temperatures contributed by rain drops are 31

540   and 51 K more than that contributed by cloud droplets at the frequencies of 23.8 and 31.4 GHz,

541   even though their LWPs are the same (1 kg m^{-2}) in these two tests.

542

543   Data availability. NOAA vertical profile radar datasets are publicly available in the DOE archives

544   (http://iop.archive.arm.gov/arm-iop/2011/sgp/mc3e/williams-s_band/). KAZR ARSCL data are

545   available on the DOE ARM archive (https://www.arm.gov/data).

546

547   Author contributions. JT and XD conceptualized this study. JT developed the retrievals, analyzed

548   the data and drafted the manuscript. XD contributed the interpretation of the results and the editing

549   of the paper. CW contributed the discussions to the methodology in rain and cloud microphysics

550   retrieval and the editing of the paper. BX and PW contributed the discussions of the results.

551

552   Competing interests. The authors declare that they have no conflict of interest

553

561

562 **References**

563 Ackerman, T. P., and Stokes, G. M: The Atmospheric Radiation Measurement Program. Phys.

564   Today, 56,38–44, doi:10.1063/1.1554135, 2003

565 Battaglia, A., Saavedra, P., T. Rose, and Simmer, C.: Characterization of precipitating clouds by

566   ground-based measurements with the triple-frequency polarized microwave radiometer

567   ADMIRARI, J. Appl. Meteorol., 49(3), 394–414, 2009

568 Battaglia, A., C. Kummerow, D. Shin, and C. Williams, 2003: Constraining Microwave

569   Brightness Temperatures by Radar Brightband Observations. J. Atmos. Oceanic

570   Technol., 20, 856-871, https://doi.org/10.1175/15200426(2003)020<0856:CMBTBR>2.0

571   .CO;2

572 Cadeddu, M. P., Liljegren, J. C., and Turner, D. D.: The Atmospheric radiation measurement

573   (ARM) program network of microwave radiometers: instrumentation, data, and retrievals,

574   Atmos. Meas. Tech., 6, 2359-2372, https://doi.org/10.5194/amt-6-2359-2013, 2013

575 Cadeddu, M. P., Marchand, R., Orlandi, E., Turner, D. D. and Mech, M. (2017). Microwave

576   Passive Ground-Based Retrievals of Cloud and Rain Liquid Water Path in Drizzling

577   Clouds: Challenges and Possibilities, IEEE Trans. Geosci. Remote Sens., vol. 55, no. 11,

578   pp. 6468-6481, doi: 10.1109/TGRS.2017.2728699

579 Crewell, S., and Löhnert, U. (2003). Accuracy of cloud liquid water path from ground-based

580   microwave radiometry 2. Sensor accuracy and synergy, Radio Sci., 38, 8042,

581   doi:10.1029/2002RS002634, 3.

582 Dubrovina, L. S.: Cloudness and precipitation according to the data of airplane soundings,

583   Gidrometeoizdat, Leningrad (in Russian), 218 pp,1982

584 Ellis, S. M., and Vivekanandan, J.: Liquid water content estimates using simultaneous S and K_a

585   band radar measurements, Radio Sci., 46, RS2021, doi:10.1029/2010RS004361, 2011

586 Fabry, F. and Zawadzki, I.: Long-Term Radar Observations of the Melting Layer of Precipitation

587   and Their Interpretation. J. Atmos. Sci., 52, 838–851, https://doi.org/10.1175/1520-

588   0469(1995)052<0838:LTROOT>2.0.CO;2, 1995

589 Fan, J., Liu, Y.-C., Xu, K.-M., North, K., Collis, S., Dong, X, and Ghan, S. J.: Improving

590   representation of convective transport for scale-aware parameterization:1. Convection and

591   cloud properties simulated with spectral bin and bulk microphysics, Journal of Geophysical

592   Research: Atmosphere, 120, 3485–3509, https://doi.org/10.1002/2014JD022142, 2015

593 Feng, Z., Dong, X. Q., Xi, B. K., Schumacher, C., Minnis, P., and Khaiyer, M.: Top-of-atmosphere

594   radiation budget of convective core/stratiform rain and anvil clouds from deep convective

595   systems. Journal of Geophysical Research, 116, D23202. https://doi.org/

596   10.1029/2011JD016451, 2011

597 Feng, Z., Leung, L. R., Houze, R. A., Jr., Hagos, S., Hardin, J., Yang, Q., Han, B. and Fan, J.:

598   Structure and evolution of mesoscale convective systems: Sensitivity to cloud

599   microphysics in convection-permitting simulations over the United States. Journal of

600   Advances in Modeling Earth Systems, 10, 1470–1494.

601   https://doi.org/10.1029/2018MS001305, 2018

602 Giangrande, S. E., Collis, S., Theisen, A. K., and Tokay, A.: Precipitation estimation from the

603   ARM distributed radar network during the MC3E campaign, J. Appl. Meteor. Climatol.,

604   doi:10.1175/JAMC-D-13-0321.1, 2014

605 Jensen, M.P., Petersen, W. A., Bansemer, A., Bharadwaj, N., Carey, L. D., Cecil, D. J, and Zipser,

606   E. J.: The Midlatitude Continental Convective Clouds Experiment (MC3E), Bulletin of the

607   American Meteorological Society. 151221073208006. https://doi.org/10.1175/BAMS-D-
608   14-00228.1, 2015

609   Leinonen, J., Moisseev, D., M. Leskinen, M., and W.A. Petersen, W.A.: A Climatology of
610   Disdrometer Measurements of Rainfall in Finland over Five Years with Implications for
611   Global   Radar   Observations.   J.   Appl.   Meteor.   Climatol.,   51,   392–404,
612   https://doi.org/10.1175/JAMC-D-11-056.1, 2012

613   Leinonen, J.: High-level interface to T-matrix scattering calculations: architecture, capabilities and
614   limitations, Opt. Express, vol. 22, issue 2, 1655-1660 doi: 10.1364/OE.22.001655, 2014

615   Liljegren, J. C., Clothiaux, E. E., Mace, G. G., Kato, S., and Dong, X.: A new retrieval for cloud
616   liquid water path using a ground-based microwave radiometer and measurements of cloud
617   temperature, J. Geophys. Res., 106(D13), 14485–14500, doi:10.1029/2000JD900817,
618   2001

619   Lebsock, M.D., L'Ecuyer, T.S. and Stephens, G.L.: Detecting the Ratio of Rain and Cloud Water
620   in Low-Latitude Shallow Marine Clouds. J. Appl. Meteor. Climatol., 50, 419–432,
621   https://doi.org/10.1175/2010JAMC2494.1, 2011

622   Matrosov, S. Y.: Assessment of radar signal attenuation caused by the melting hydrometeor layer.
623   IEEE Trans. Geosci. Remote Sens., 46,1039–1047 doi: 10.1109/TGRS.2008.915757, 2008

624   Matrosov, S. Y.: A method to estimate vertically integrated amounts of cloud ice and liquid and
625   mean rain rate in stratiform precipitation from radar and auxiliary data, J. Appl. Meteor.
626   Climatol., 48, 1398–1410, doi:10.1175/2009JAMC2196.1, 2009

627   Matrosov, S. Y.: Synergetic use of millimeter- and centimeter-wavelength radars for retrievals of
628   cloud   and   rainfall   parameters,   Atmos.   Chem.   Phys.,   10,   3321-3331,
629   https://doi.org/10.5194/acp-10-3321-2010, 2010

630   Mazin, I. P. (Ed.): Clouds and the Cloudy Atmosphere. Gidrometeoizdat, Leningrad, 648 pp, 1989.

631   Saavedra, P., Battaglia, A., and Simmer, C.: Partitioning of cloud water and rainwater content by

632   ground-based observations with the Advanced Microwave Radiometer for Rain

633   Identification (ADMIRARI) in synergy with a micro rain radar, J. Geophys. Res., 117,

634   D05203, doi:10.1029/2011JD016579, 2012

635   Sassen, K., Campbell, J. R., Zhu, J., Kollias, P., Shupe, M., and Williams, C.: Lidar and Triple-

636   Wavelength Doppler Radar Measurements of the Melting Layer: A Revised Model for

637   Dark-   and   Brightband   Phenomena.   J.   Appl.   Meteor.,   44,   301–312,

638   https://doi.org/10.1175/JAM-2197.1, 2005

639   Sheppard, B.E.: Effect of Rain on Ground-Based Microwave Radiometric Measurements in the

640   20–90-GHz   Range.   *J.   Atmos.   Oceanic   Technol.,*   13,   1139–1151,

641   https://doi.org/10.1175/1520-0426(1996)013<1139:EOROGB>2.0.CO;2, 1996

642   Tian, J., Dong, X., Xi, B., Wang, J., Homeyer, C. R., McFarquhar, G. M., and Fan J.: Retrievals

643   of ice cloud microphysical properties of deep convective systems using radar

644   measurements, Journal of Geophysical Research: Atmosphere., 121,10 ,820–10,839,

645   https://doi.org/10.1002/2015JD024686, 2016

646   Tian, J., Dong, X., Xi, B., Minnis, P., Smith, W. L., Jr, Sun-Mack, S., Thieman, M., Wang, J.:

647   Comparisons of ice water path in deep convective systems among ground-based, GOES,

648   and CERES-MODIS retrievals. Journal of Geophysical Research: Atmospheres, 123,

649   1708–1723. https://doi.org/10.1002/2017JD027498, 2018

650   Tridon, F., and Battaglia, A.: Dual-frequency radar Doppler spectral retrieval of rain drop size

651   distributions and entangled dynamics variables, J. Geophys. Res. Atmos., 120, 5585–5601,

652   doi:10.1002/2014JD023023, 2015

653   Tridon, F., Battaglia, A., and Kollias, P.: Disentangling Mie and attenuation effects in rain using a

654   Ka-W dual-wavelength Doppler spectral ratio technique, Geophys. Res. Lett., 40, 5548

655   5552, doi:10.1002/2013GL057454, 2013

656   Tridon, F., Battaglia, A., Luke, E., and Kollias, P.: Rain retrieval from dual-frequency radar

657   Doppler spectra: validation and potential for a 25 midlatitude precipitating case-study,

658   Quarterly Journal of the Royal Meteorological Society, 143, 1364–1380, 2017.

659   Turner, D. D., Clough, S. A., Liljegren, J. C., Clothiaux, E. E., Cady-Pereira, K. E., and Gaustad,

660   K. L.: Retrieving liquid water path and precipitable water vapor from the Atmospheric

661   Radiation Measurement (ARM) microwave radiometers. IEEE Trans. Geosci. Remote

662   Sens., 45, 3680–3690, 2007

663   Wentz, F.J. and Spencer, R.W.: SSM/I Rain Retrievals within a Unified All-Weather Ocean

664   Algorithm. J. Atmos. Sci., 55, 1613–1627, https://doi.org/10.1175/1520-

665   0469(1998)055<1613:SIRRWA>2.0.CO;2, 1998

666   Williams, C. R.: Reflectivity and liquid water content vertical decomposition diagrams to diagnose

667   vertical evolution of raindrop size distributions, J. Atmos. Oceanic Technol.,

668   doi:10.1175/JTECH-D-15-0208.1, 2016

669   Williams, C. R., Beauchamp, R. M., and Chandrasekar, V.: Vertical air motions and raindrop size

670   distributions estimated from mean Doppler velocity difference from 3- and 35-GHz

671   vertically pointing radars. IEEE Trans. Geosci. Remote Sens., 54, 6048–6060,

672   https://doi.org/10.1109/ TGRS.2016.2580526, 2016

673   Xu, W.: Precipitation and convective characteristics of summer deep convection over east Asia

674   observed by TRMM, Monthly Weather Review., 141, 1577-1592.

675   https://doi.org/10.1175/MWR-D-12-001

676

677 **Table 1**. Acronyms and Abbreviations Used in This Study

Acronyms and Abbreviations	Full Name
2DVD	Two-dimensional video disdrometer
A	Total two-way attenuation of 35-GHz VPR signals
ARSCL	Active remote sensing of clouds
ARM	Atmospheric Radiation Measurement
B	coefficients for cloud water attenuation
C	coefficients for rainfall attenuation
CLWP	Cloud liquid water path
D	Raindrop diameter
D_m	Mean mass-weighted raindrop diameter
D_{max}	Maximum diameters in the size distribution
D_{min}	Minimum diameters in the size distribution
DOE	Department of Energy
DSD	Drop size distribution
DVD	Doppler velocity difference
G	Two-way gaseous absorption
IWC	Ice water content
KAZR	Ka-band ARM zenith radar
LUT	Looking up table
LWP	Liquid water path
MB	Base of melting layer
MC3E	Mid-latitude continental convective clouds experiment
MMCR	Millimeter-wavelength cloud radar
MWR	Microwave radiometer
N_{DSD}	Number concentration
N_0	Intercept of ice particle size distribution
NOAA	National Oceanic and Atmospheric Administration
N_w	Scaling parameter in the drop size distribution
RLWP	Rain liquid water path
R_m	Layer-mean rain rate
RR	Rain rate

$\mathbf{S_{DSD}^{\lambda}}$	Radar reflectivity-weighted velocity spectral density
$\mathbf{v_{DSD}^{\lambda}}$	First reflectivity-weighted velocity spectrum moments represent the mean velocity
$\mathrm{V_Z}$	Raindrop terminal velocity
$\mathbf{Z_{DSD}^{\lambda}}$	Zeroth reflectivity-weighted velocity spectrum moments represent the intrinsic (non-attenuation) reflectivity factor
$\mathbf{\Gamma(x)}$	Euler gamma function
λ	Radar wavelength
$\mathbf{\sigma_b^{\lambda}}$	Raindrop backscattering cross section
μ	Shape parameter

678

679

680 **Table 2.** Statistics (mean differences, 95% confidence interval of mean differences, RMSEs) of D_m, RR between this study (RET) and
681 disdrometers (2DVD, RD-80) for Case A and Case B
682
683
684
685
686
687

	Mean Differences (95% confidence interval)	RMSE
Case A: D_m (RET, 2DVD) (mm)	0.04 (-0.07, -0.01)	0.24
Case A: RR (RET, RD-80) (mm hr^{-1})	-0.45 (-0.57, -0.33)	0.96
Case A: RR (RET, 2DVD) (mm hr^{-1})	-0.61(-0.77, -0.43)	1.38
Case B: D_m (RET, 2DVD) (mm)	0.10 (-0.14, -0.07)	0.27
Case B: RR (RET, RD-80) (mm hr^{-1})	0.40 (0.19, 0.60)	1.51
Case B: RR (RET, 2DVD) (mm hr^{-1})	0.30(0.09, 0.52)	1.58

688   **Table A.** The brightness temperatures (TB) at 23.8 and 31.4 GHz for different assumptions of CLWP and RLWP values.

Sensitivity Test	CLWP (kg m^{-2})	RLWP (kg m^{-2})	TB at 23.8 GHz	TB at 31.4 GHz
#1	2	0	197.20	196.28
#2	1	0	186.34	177.49
#3	0	1	217.28	228.20
#4	0	2	254.51	272.09
#5	1	1	225.37	239.88

689

690

691

692
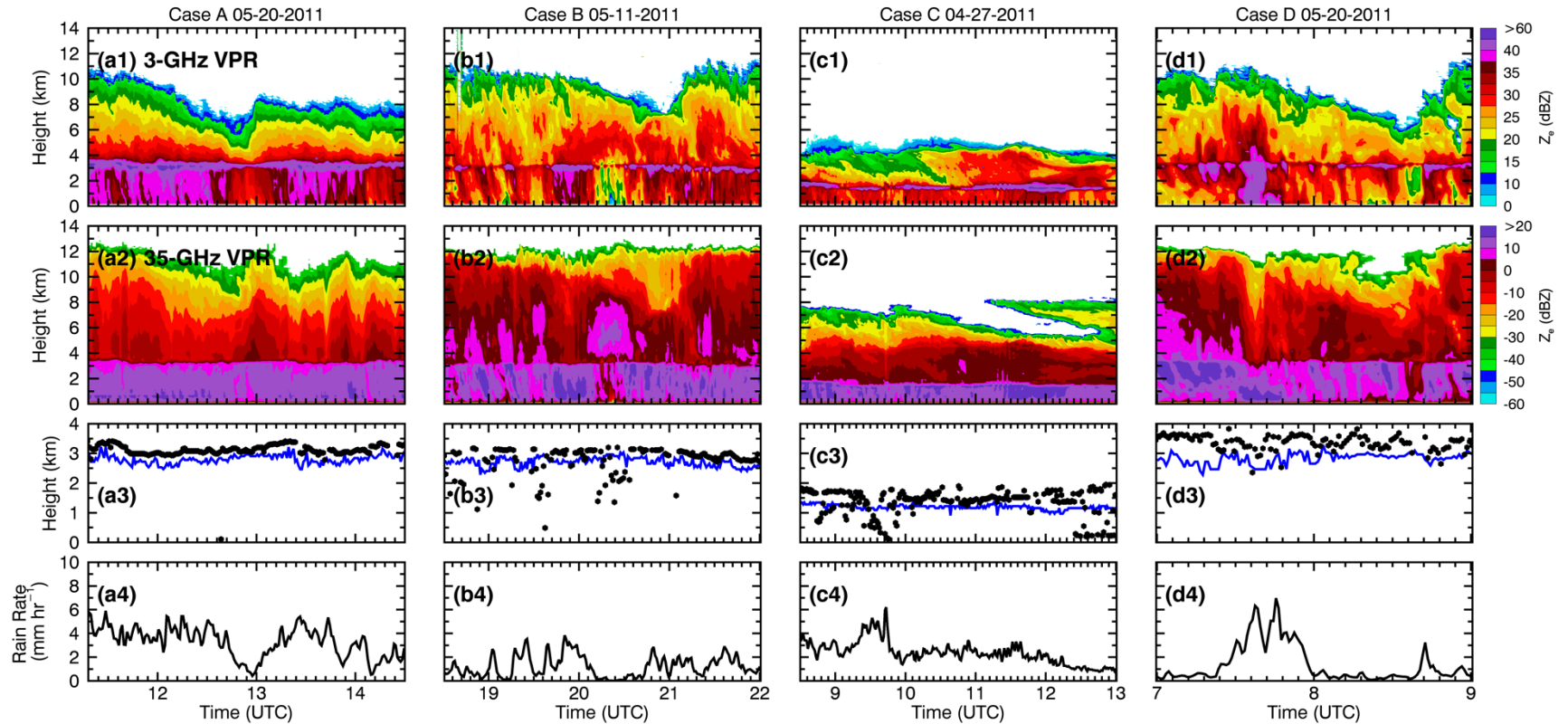
Figure 1. Time series of (a1) radar reflectivity (Z_e) from NOAA 3-GHz vertical pointing radar (VPR), (b1) radar reflectivity from ARM 35-GHz VPR, (c1) melting base (blue lines) and cloud base (black dots), and (d1) rain rates from RD-80 surface disdrometer measurement for Case A (20 May 2011, 11:20 – 14 :30 UTC); (b1)-(b4) for Case B (11 May 201, 18:30 – 22 :00 UTC); (c1)-(c4) for Case C (27 April 2011, 8:30 – 13 :00 UTC); (d1)-(d4) for Case D (20 May 2011, 7:00 – 9 :00 UTC). Note that the ranges of radar dBZ values are different in 3-GHz and 35-GHz radars.

698
699
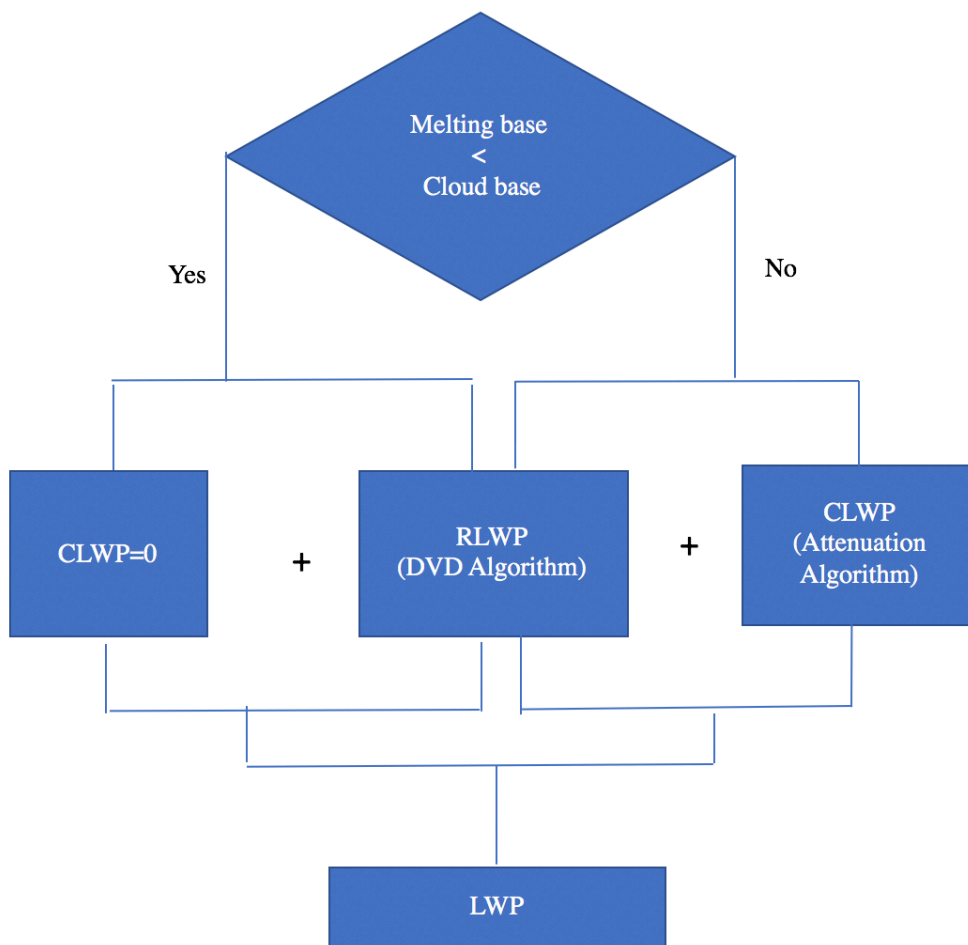
700

701 **Figure 2**. Algorithm flowchart to retrieve liquid water path (LWP) below melting base.

702

703
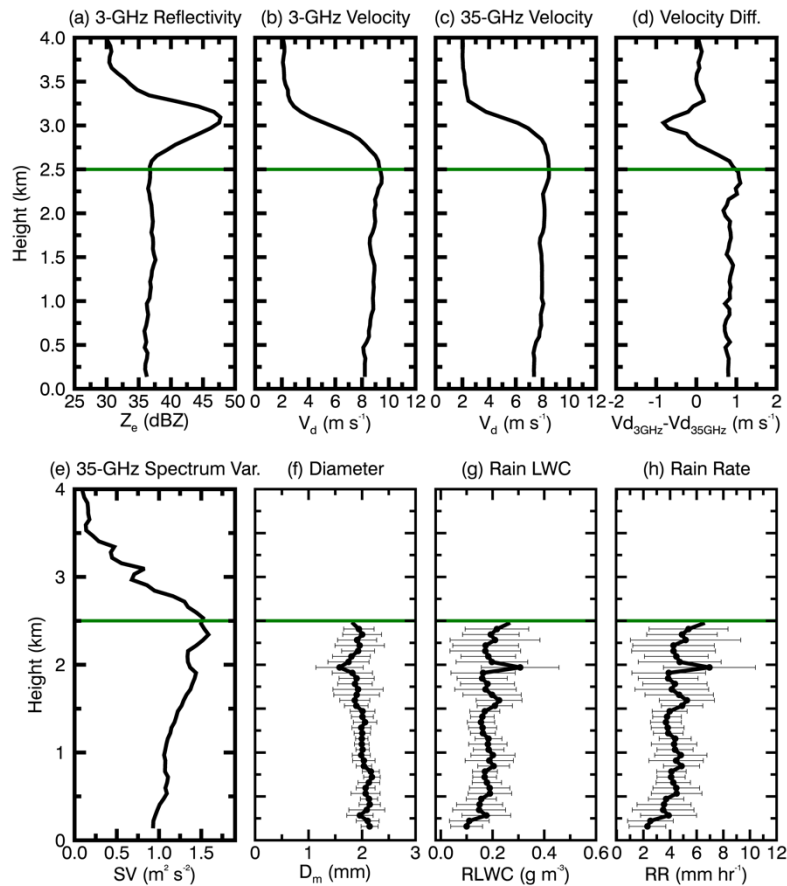
704

705   **Figure 3**. An example of illustrating the Doppler Velocity Differences (DVD) retrieval algorithm
706   at 13:40 UTC on May 20, 2011. The inputs of the DVD retrieval algorithm are: (a) 3-GHz vertical
707   pointing radar reflectivity factor (Z_e), (b) 3-GHz radar Doppler velocities (V_d), (c) 35-GHz radar
708   Doppler velocities (V_d), and (e) 35-GHz radar spectrum variances (SV). The Doppler velocity
709   difference between 3-GHz and 35 GHz is shown in (d). The outputs of the DVD retrieval
710   algorithm are: (f) mass-weighted mean diameter D_m, (g) rain liquid water content (RLWC), and
711   (h) rain rate (RR). Retrieval uncertainties are shown as horizontal thin black lines.
712

713
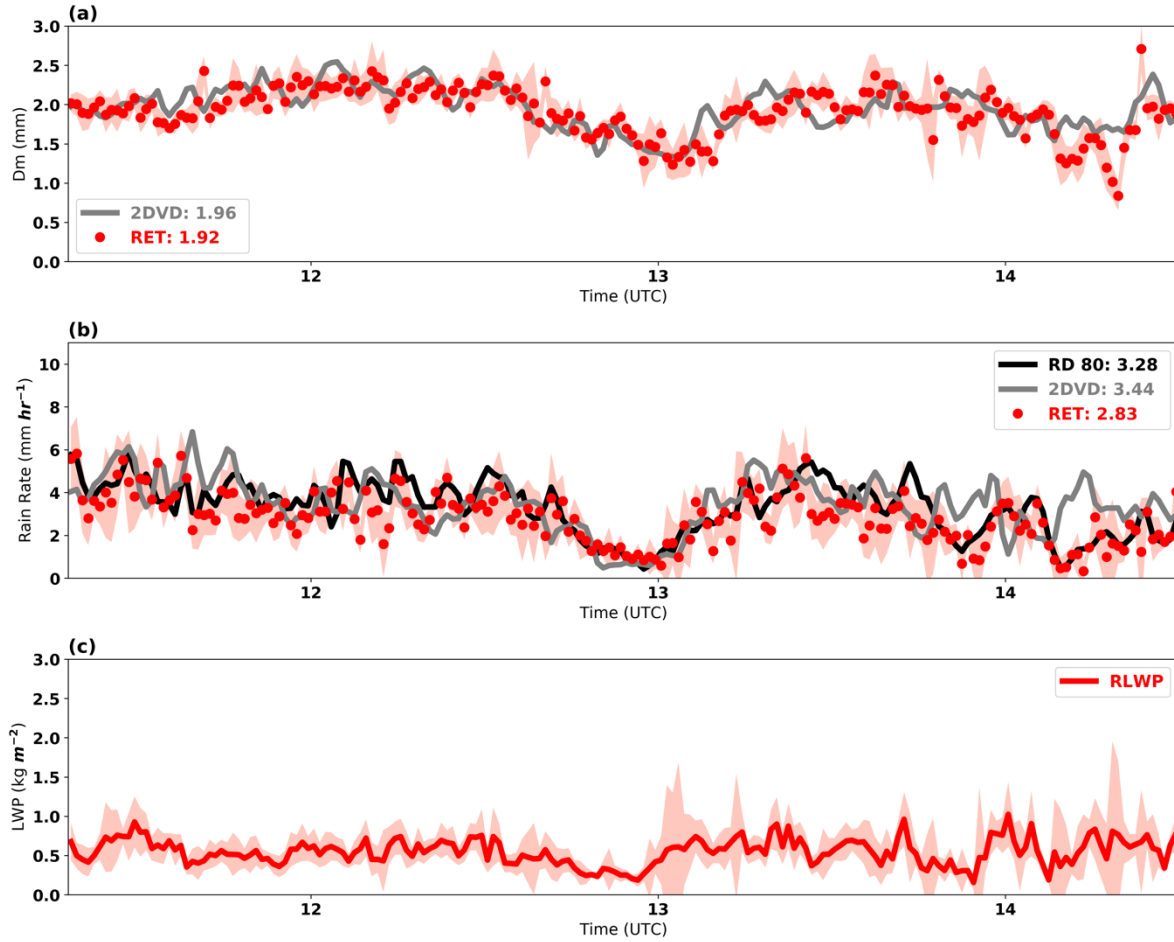
Figure 4. Time series of (a) retrieved (RET) (red dots) and 2DVD surface disdrometer estimated
(grey line) D_m, (b) RET (red line), 2DVD (grey line) and RD-80 (black line) surface disdrometer
rain rate estimates, and (c) retrieved rain liquid water path (RLWP, red dots) for Case A (May 20,
2011. The red shading areas are the estimated retrieval uncertainties.

718

719
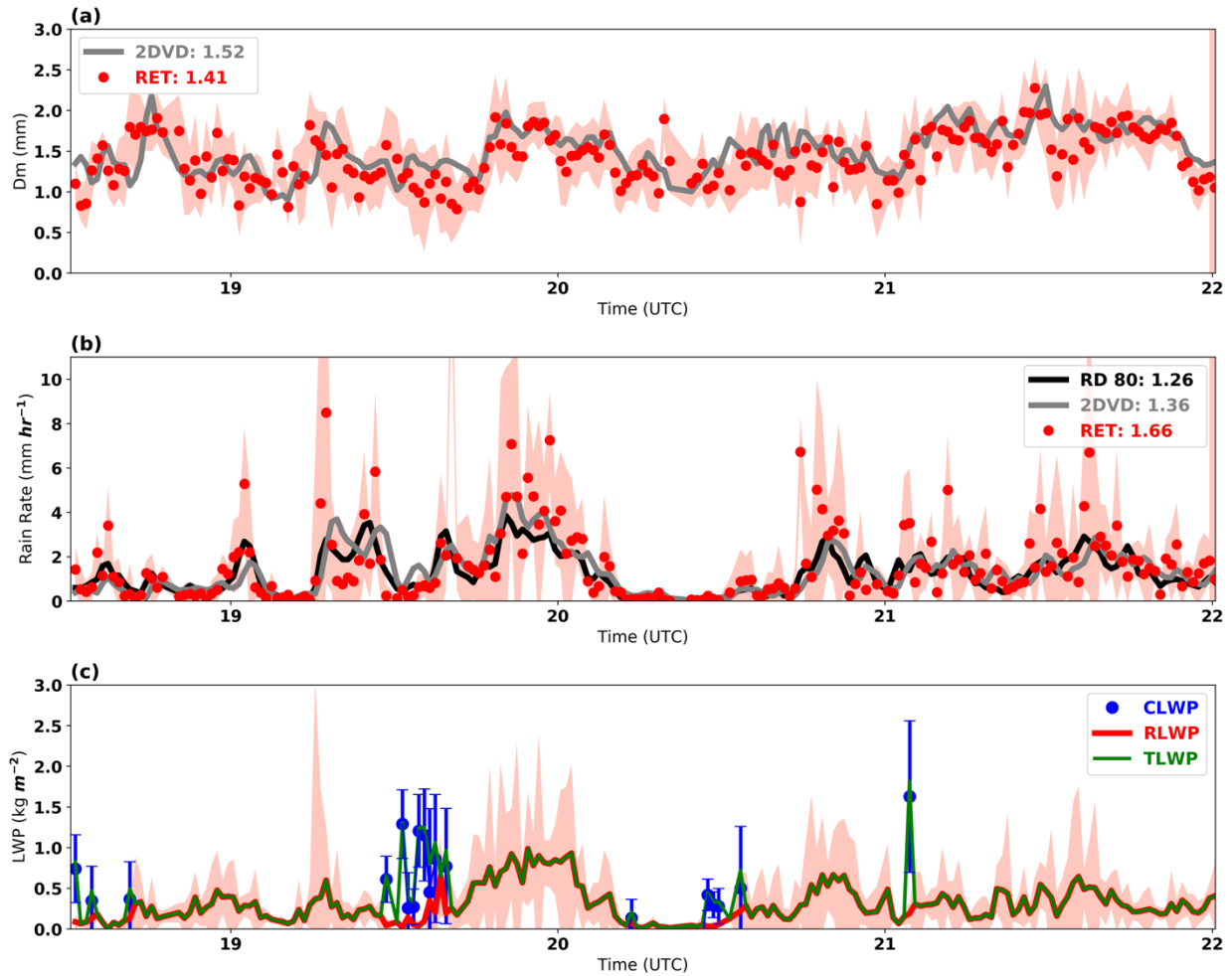
Figure 5. Time series of (a) retrieved (RET) (red dots) and 2DVD surface disdrometer estimated
(grey lines) D_m, (b) RET (red dots), 2DVD (grey line) and RD-80 (black line) surface disdrometer
rain rate estimates, and (c) rain liquid water path (RLWP, red line), cloud liquid water path (CLWP,
blue dots) and liquid water path (LWP = RLWP+CLWP, green lines) for Case B (May 11, 2011).
The red shading area and blue bars are the estimated retrieval uncertainties for rain microphysical
properties (D_m, rain rate and RLWP) and CLWP.
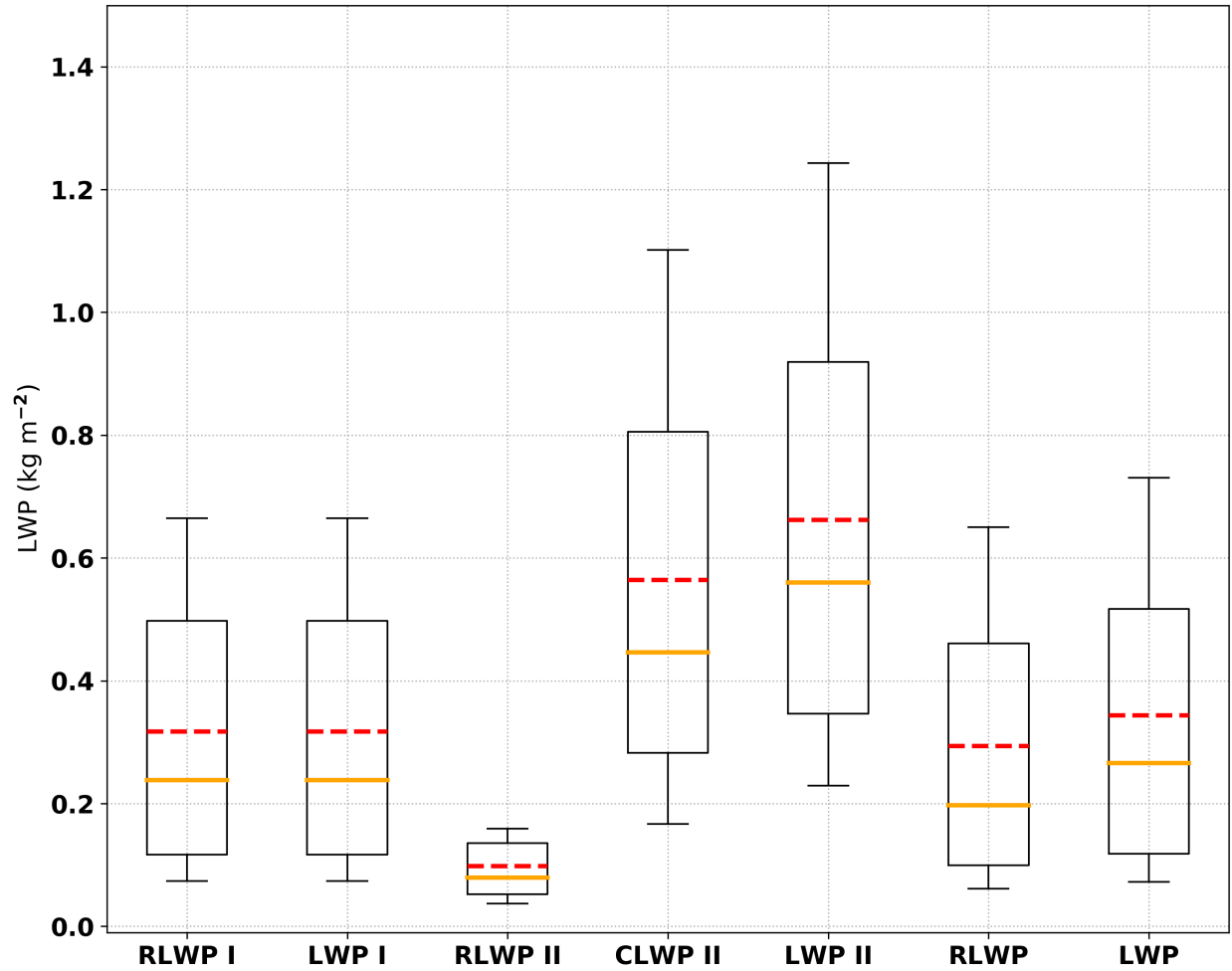
Figure 6. Box and whisker plots of retrieved RLWP, CLWP and LWP for situation (I), (II) and all samples. The horizontal orange line within the box indicates the median, boundaries of the box represent the 25th- and 75th -percentile, and the whiskers indicate the 10th- and 90th -percentile values of the results. The red dash lines represent the mean values.
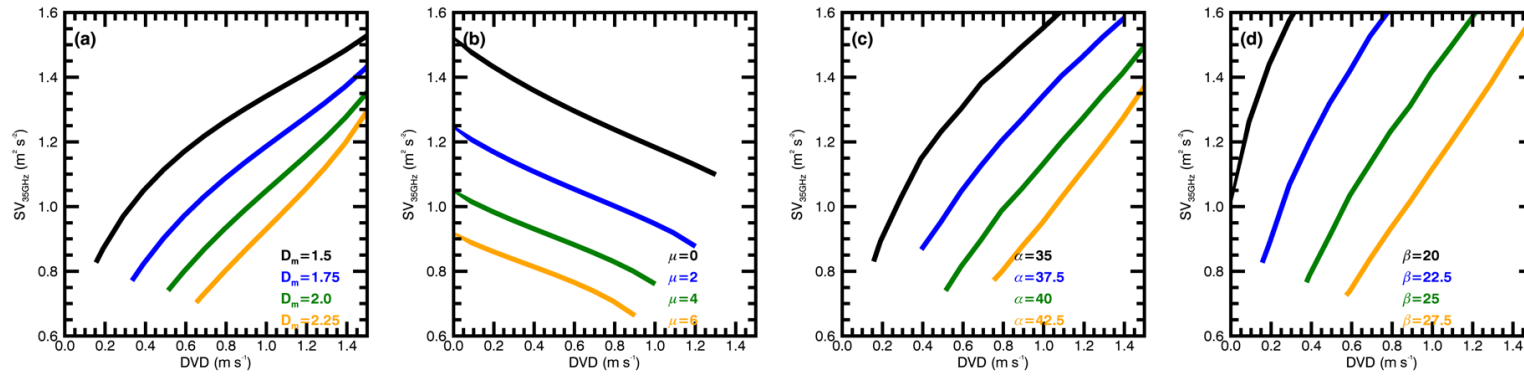
733
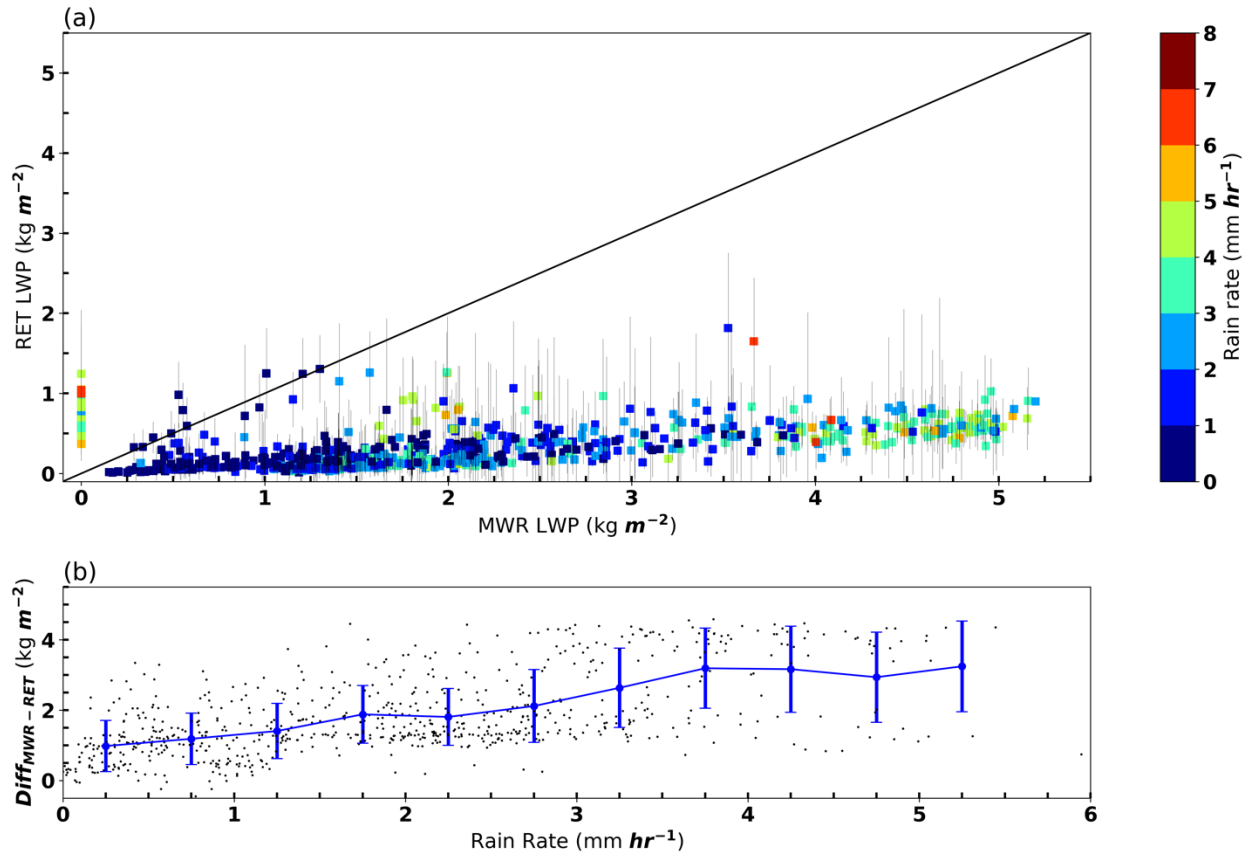
734

735   **Figure 7**. (a) Comparisons between LWP from microwave radiometer (MWR, in x-axis) and LWP
736   retrievals from this study (RET, in y-axis, with estimated uncertainty in gray lines). The rain rates
737   are indicated by colors. (b) the LWP differences between two estimations (MWR- RET), shown
738   as a function of rain rate.

739

Figure A. Comparisons of (a) mass-weighted mean diameter D_m (mm), (b) shape parameter μ, (c) parameter $\alpha = 10 \log(Z_{3GHz}/RLWC)$, and (d) parameter $\beta = 10 \log(Z_{3GHz}/RR)$ calculated as functions of Doppler velocity difference (DVD) and spectrum variance at 35 GHz (SV_{35GHz}). Note that the units of RLWC and RR are g m^{-3} and mm hr^{-1}.

743
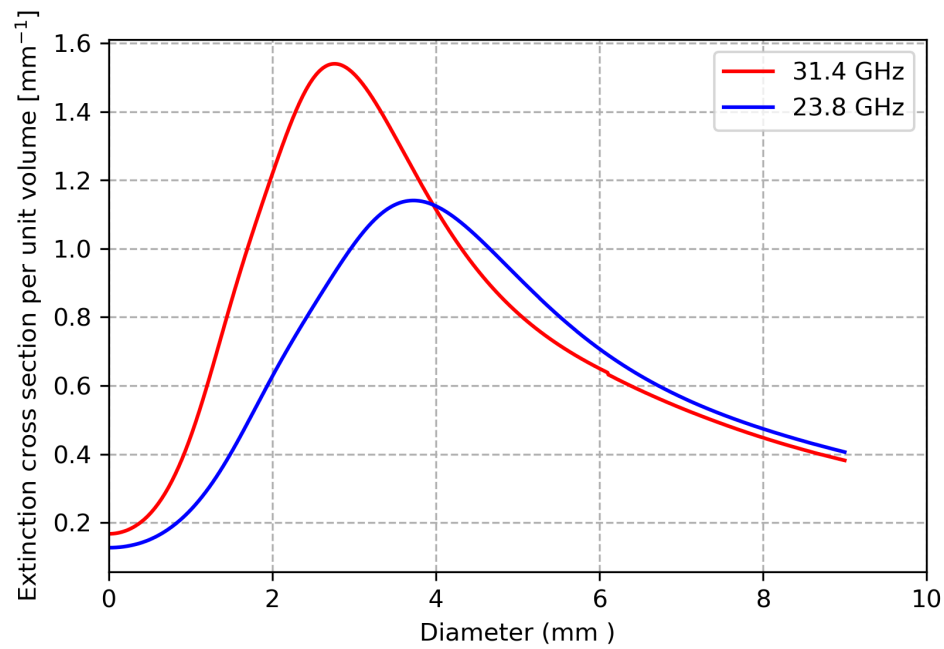
Figure B. The extinction cross section per unit volume as a function of the drop equivolume diameter for the two frequencies in MWR (23.8 GHz and 31.4 GHZ).

746
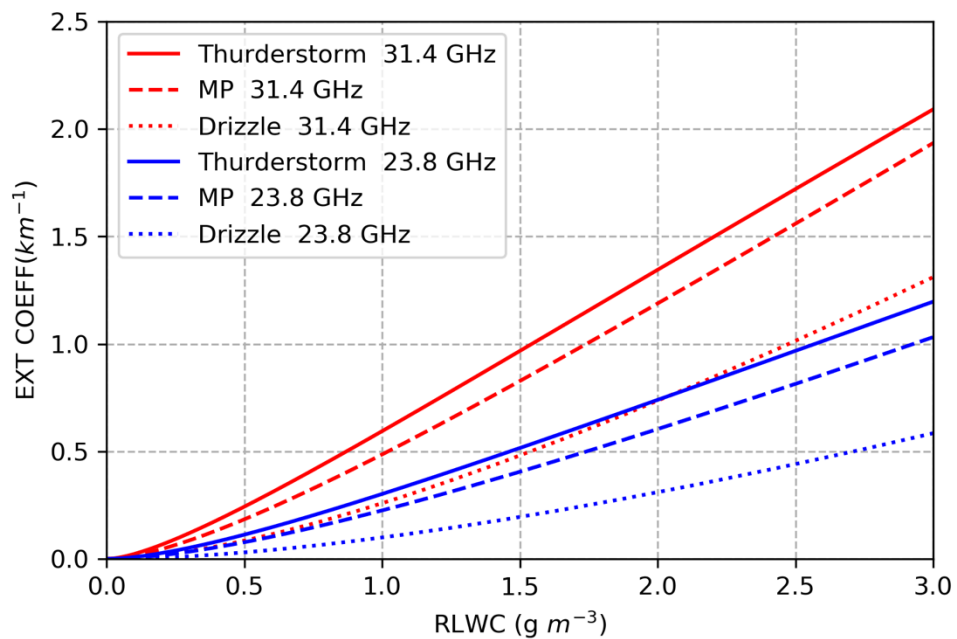
Figure C. The extinction coefficient as a function of RLWC for precipitations with three different drop size distributions (DSDs), which are for heavy precipitation (thunderstorm), moderate precipitation (MP) and drizzle precipitation (drizzle).

749
750